

Complex Interplay between Absorber Composition and Alkali Doping in High-Efficiency Kesterite Solar Cells

Stefan G. Haass,* Christian Andres, Renato Figi, Claudia Schreiner, Melanie Bürki, Yaroslav E. Romanyuk, and Ayodhya N. Tiwari

Sodium treatment of kesterite layers is a widely used and efficient method to boost solar cell efficiency. However, first experiments employing other alkali elements cause confusion as reported results contradict each other. In this comprehensive investigation, the effects of absorber composition, alkali element, and concentration on optoelectronic properties and device performance are investigated. Experimental results show that in the row Li–Na–K–Rb–Cs the nominal Sn content should be reduced by more than 20% (relative) to achieve the highest conversion efficiency. The alkali concentration resulting in highest device efficiencies is lower by an order of magnitude for the heavy alkali elements (Rb, Cs) compared to the lighter ones (Li, Na, K). Utilization of a wide range of characterization techniques helps to unveil the complex interplay between absorber composition and alkali doping. A ranking of alkali for best device performances, when employing alkali treatment, resulted in the order of $\text{Li} > \text{Na} > \text{K} > \text{Rb} > \text{Cs}$ based on the statistics of more than 700 individual cells. Finally, a champion device with 11.5% efficiency (12.3% active area) is achieved using a high Li concentration with an optimized Sn content.

1. Introduction

Kesterite ($\text{Cu}_2\text{ZnSn}(\text{S,Se})_4$ (CZTSSe)) solar cells see an increased research interest after the recent announcement of a new record efficiency of 13.7%^[1] for this thin-film technology based on earth-abundant elements. The relatively low open-circuit voltage, which is often described quantitatively as $V_{\text{OC-deficit}}$ ($V_{\text{OC-deficit}} = E_g - V_{\text{OC}}$), still remains the major problem inhibiting further efficiency improvement despite the excellent potential of the

kesterite material with its optimal bandgap and absorption coefficient.^[2] Alkali treatment of kesterite solar cells is one of the measures to reduce the high $V_{\text{OC-deficit}}$ and most of today's >10% efficiency kesterite devices utilize the beneficial effects of alkali elements on absorber layer morphology and optoelectronic properties. So far the most research attention has been paid to sodium, resulting in many thorough investigations which revealed grain size enhancement, passivation of grain boundaries, and an increase in net hole concentration as the major beneficial effects of sodium treatments.^[3–6] Also lithium addition has shown to improve device performance by boosting the electronic quality of the CZTSSe absorber material and grain boundaries.^[7] First studies on the effect of potassium addition confirmed advantageous effects on kesterite absorber growth and optoelectronic properties similar to


Na.^[8,9] Several studies comparing different alkali elements and their effect on solar cell properties and device performance have recently been published.^[10–13] Table 1 compares the effects on device performance by extracting a ranking of the various alkali elements in each publication in the order of their capability to improve device performance. It is apparent from these rankings that no consistent experimental results have been obtained, which triggers two questions: (i) Why do the published results differ so much? (ii) Which alkali element possesses the highest potential for efficiency improvements?

This paper aims to unveil the discrepancy between the recently published results comparing the effects of alkali treatments on device performance. Our hypothesis is that each alkali element requires a different absorber composition to achieve the highest PV performance and we therefore prepared a comprehensive set of samples with different alkali elements and alkali concentrations as well as various metal ratios. All samples were thoroughly characterized by scanning electron microscopy (SEM), X-ray diffraction (XRD), X-ray fluorescence (XRF), inductively coupled plasma-mass spectrometry (ICP-MS), as well as current–voltage (J – V), capacitance–voltage (C – V), time-resolved photoluminescence (TRPL), and external quantum efficiency (EQE) measurements.

The methodology used for absorber synthesis is based on the solution process described elsewhere,^[14] allowing for accurate alkali incorporation by simply adding alkali chlorides to the solution.^[15] Figure 1a illustrates the matrix of sample compositions prepared with five different alkali elements: lithium (Li),

S. G. Haass, C. Andres, Dr. Y. E. Romanyuk, Prof. A. N. Tiwari
Laboratory for Thin Films and Photovoltaics
Empa – Swiss Federal Laboratories for Materials Science and Technology
Ueberlandstrasse 129, 8600 Dübendorf, Switzerland
E-mail: stefan.haass@empa.ch

R. Figi, C. Schreiner, M. Bürki
Laboratory for Advanced Analytical Technologies
Empa – Swiss Federal Laboratories for Materials Science and Technology
Ueberlandstrasse 129, 8600 Dübendorf, Switzerland

 The ORCID identification number(s) for the author(s) of this article can be found under <https://doi.org/10.1002/aenm.201701760>.

© 2017 The Authors. Published by WILEY-VCH Verlag GmbH & Co. KGaA, Weinheim. This is an open access article under the terms of the Creative Commons Attribution-NonCommercial License, which permits use, distribution and reproduction in any medium, provided the original work is properly cited and is not used for commercial purposes.

The copyright line for this article was changed on 8 Dec 2017 after original online publication.

DOI: 10.1002/aenm.201701760

Table 1. List of recent publications comparing the effects of alkali elements on the device performance of kesterite solar cells.

Reference	Order of performance improvement
"Effect of different alkali (Li, Na, K, Rb, Cs) metals on $\text{Cu}_2\text{ZnSnSe}_4$ solar cells" ^[10]	$\text{Na} > \text{Cs} > \text{K} > \text{Rb} > \text{Li}$
"Efficiency enhancement of $\text{Cu}_2\text{ZnSn}(\text{S},\text{Se})_4$ solar cells via alkali metals doping" ^[11]	$\text{K} > \text{Rb} > \text{Na} > \text{Li} > \text{Cs}$
"Influence of alkali metals (Na, Li, Rb) on the performance of electrostatic spray-assisted vapor deposited $\text{Cu}_2\text{ZnSn}(\text{S},\text{Se})_4$ solar cells" ^[12]	$\text{Li} > \text{Na} > \text{Rb}$
"Alkali doping strategies for flexible and light-weight $\text{Cu}_2\text{ZnSnSe}_4$ solar cells" ^[13]	$\text{K} > \text{Na}$

sodium (Na), potassium (K), rubidium (Rb), and cesium (Cs). The nominal alkali concentration was varied in three steps of 0, 10, and 100 mM in the precursor solution which corresponds to 0, 0.33, and 3.33 at% relative to all absorber elements. Variations in the metal ratios were put into effect by changing the Sn concentration in the precursor solution in up to 12 steps yielding overall more than 80 samples and thus >700 individual cells. From the Sn content in the absorber layer measured by XRF and ICP-MS (Figure S1, Supporting Information) we conclude that the Sn loss is proportional to the overall nominal Sn content and that it is invariant under the addition of various alkali elements as well as their concentrations. The Cu/(Zn+Sn) and Zn/Sn ratios, both nominal and XRF measurements on the selenized absorber, are shown in Figure S8a,b (Supporting Information).

Alkali content was analyzed in the absorber layer of the full devices by ICP-MS and compared to the nominal input. Figure 1b shows the measured concentration of all five alkali elements in the two nominal concentrations. The concentrations represent the alkali element that was intentionally added to the specific sample (Li in the Li sample and so on). The ICP-MS measurements show that intentionally added alkali elements are successfully incorporated into the absorber layer and a higher nominal alkali concentration corresponds to a higher measured alkali content by ICP-MS. However, the majority of the alkali amount escapes during the processing, which could take place during the spin-coating process (subsequent layers can dissolve

preferentially alkali-chloride crystals from the antecedent layer and wash them off) or during the chemical bath deposition of the CdS buffer layer because of the high solubility of alkali compounds in water. Furthermore, the results of ICP-MS measurements reveal that heavier alkali elements remain at higher concentrations inside the absorber layer than lighter elements, except for the case of Li. As the alkali elements are preferably located along the grain boundaries,^[16,17] the overall amount measured by ICP-MS, which does not discriminate between alkali elements inside grains or in the grain boundaries, is expected to be higher for samples with a higher density of grain boundaries.

In the following, we will always refer to the nominal values of $\text{Sn}/(\text{Cu}+\text{Zn}+\text{Sn})$ in at% because the step size of variations is smaller than the error margins of the compositional measurements by XRF. We will refer to the 10 mM (0.33 at%) and 100 mM (3.33 at%) alkali containing samples as to "low" and "high" alkali content, respectively.

2. Results and Discussion

The main findings of this study are aggregated in **Figure 2** which shows the device efficiency as a function of the nominal Sn content (y-axis) and the alkali elements from Li to Cs with the "high" alkali content (x-axis). The color code resembles the average efficiency of nine cells (designated illumination area measurement) and the stars indicate the Sn content yielding the highest efficiency for a given alkali element. The highest device efficiency for each alkali element increases from 6.5% for Cs to more than 10.5% for Li. The optimal Sn content that results in the best efficiency increases concurrently from 26.5% for Cs up to 33.3% for Li. The range of Sn content that yields comparable high efficiency is dependent on the alkali element and narrows down from Li to Na to K. The average efficiencies in the case of Rb and Cs are only weakly dependent on the Sn content and therefore exhibit a comparably homogenous efficiency distribution, however resulting in overall lower device efficiency values. The reduction of efficiency at high and low Sn contents that is most prominent for Li, Na, and K can be attributed to the formation of secondary phases which deteriorate FF, V_{OC} , and J_{SC} . Strikingly, the dependency of the Sn content on the highest device performance of different alkali elements

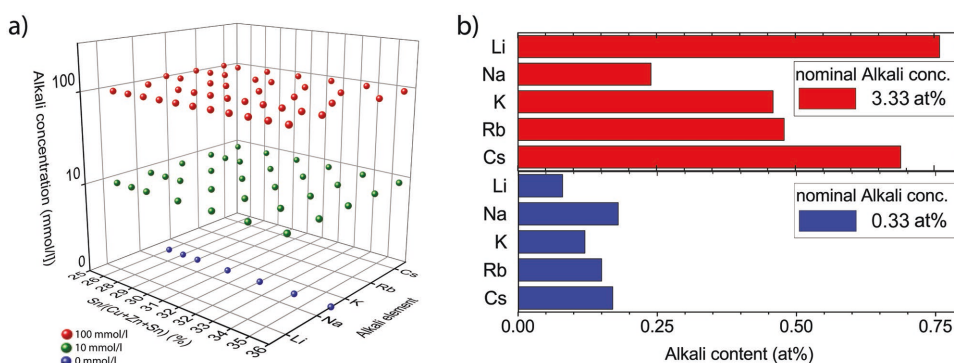


Figure 1. a) All samples fabricated for this study are depicted in dependence of the alkali element, alkali concentration, and Sn content. b) Comparison of the nominal alkali concentration with the alkali content determined by ICP-MS measurements.

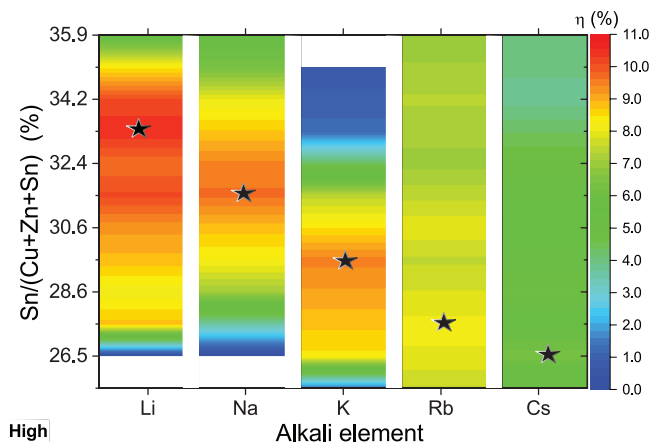


Figure 2. Device efficiency averaged over nine cells as a function of the nominal Sn content and the alkali element from Li to Cs for “high” concentration. The color code resembles the efficiency up to 11% and the stars indicate the Sn content yielding highest efficiency for a given alkali element.

has neither been reported before nor taken into account in earlier publications that compared the effects of alkali elements on kesterite solar cells.^[10–13]

The influence of Sn content on V_{OC} , J_{SC} , and FF is shown in Figure 3a–c for the “high” alkali content samples. As a result of the qualitatively distinct behavior of Li, Na, and K

(light alkali elements) on the one hand and Rb and Cs (heavy alkali elements) on the other, it is helpful to separate them into two groups. The maximum V_{OC} for a given alkali element increases from K to Na to Li while simultaneously the maximum J_{SC} decreases, which will be addressed later. Rb exhibits intermediate values for both V_{OC} and J_{SC} and Cs comparably low values. The FF shows highest values of up to 65% for Li while the other alkali elements can yield values up to 60%. The optimal Sn content for highest FF coincides with the highest efficiency in Figure 2. The degradation of FF at high Sn contents is associated with the appearance of $\text{Sn}(\text{S},\text{Se})_2$ secondary phase that segregates on top of the samples (Figure S2, Supporting Information) and appears at Cu/Sn ratio < 1.65 in the absorber as measured by XRF.^[18] At low Sn concentrations the devices show a degradation of V_{OC} , J_{SC} , and FF simultaneously, which is caused by shunting due to the formation of Cu_2Se phases which occur at Cu/Sn ratios > 2.0 measured by XRF.^[19]

The bandgap trends of the kesterite layers are presented in Figure 3d as derived from the inflection point in the long wavelength region of the EQE.^[20] An increase in nominal Sn content correlates with a concurrent increase in bandgap. The increase in bandgap can be attributed to the change of metal ratios resulting in an increase in ordering of the Cu/Zn sublattice.^[21] Because of the abundance of Zn in the absorber layer composition an increase in Sn concentration results in the formation of kesterite phase material with a lower Cu content.

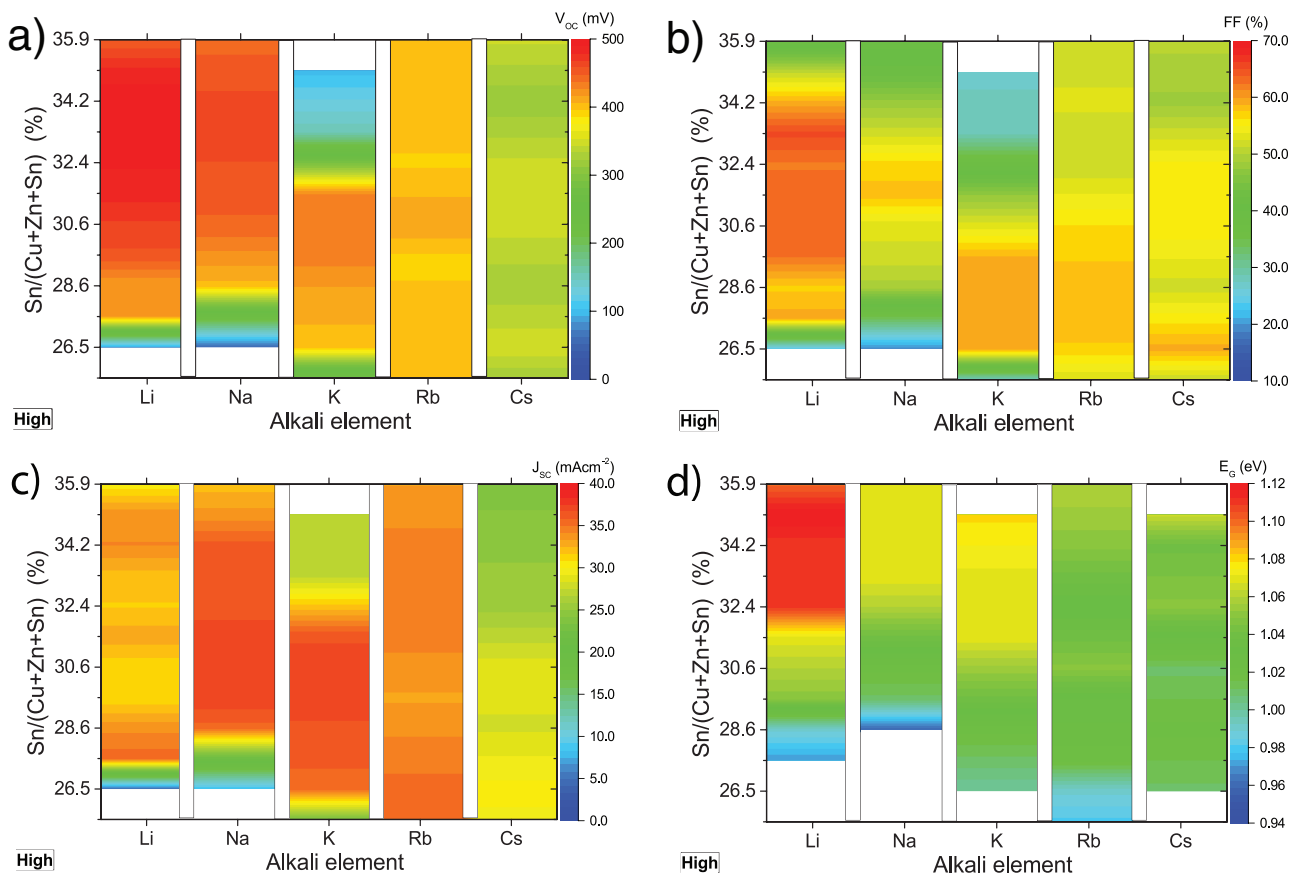


Figure 3. a) V_{OC} , b) FF, and c) J_{SC} for the “high” alkali content samples. d) Bandgap E_g for the same samples. The bandgap is determined from the inflection point of the EQE in the long wavelength region.

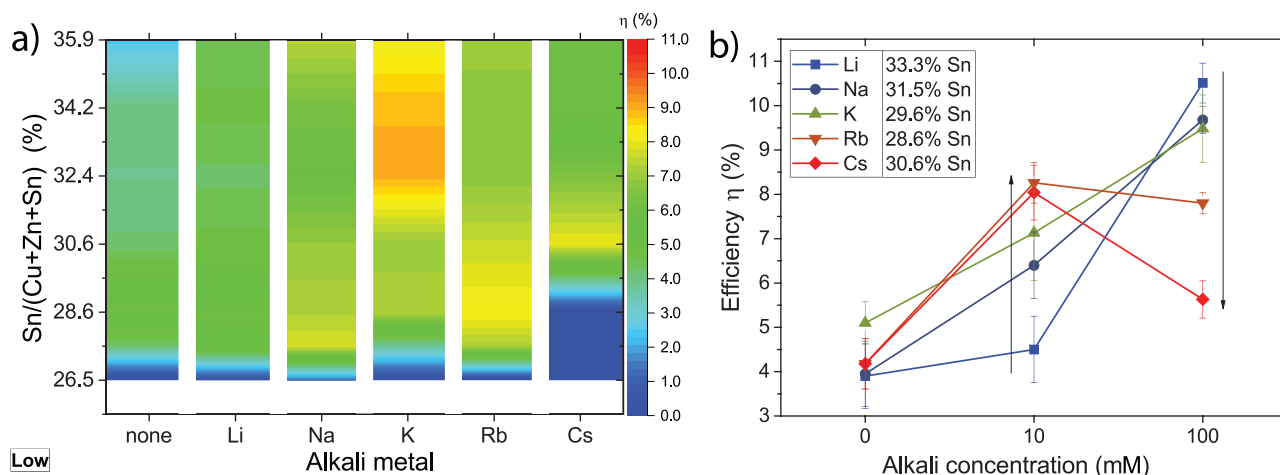


Figure 4. a) The average efficiency of nine cells for none and “low” alkali content samples. b) Evolution of efficiency from 0 to low to high alkali content for a specific Sn content. The required alkali concentration for maximum device performance is lower for heavier alkali elements.

The change of the kesterite phase composition can explain the bandgap change for Na and K addition but Li, Rb, and Cs exhibit a different behavior. Li-containing samples exhibit a sudden increase of the bandgap for Sn nominal concentrations above 31.5% meaning that the bandgap change is taking place once the kesterite composition is considerably Cu poor and is associated with an incorporation of Li onto Cu sites inside the kesterite lattice.^[22] Incorporation of Li into the CZTSe lattice was reported to increase the bandgap and we assume that in the case of thin film synthesis a notable amount of Li can only be incorporated into the lattice if the chemical potential of Cu is lower than a certain threshold. The substitution energy for Li_{Cu} in CZTSe is reported to be 0.27 eV in contrast to Na and K with 0.55 and 1.55 eV, respectively.^[23] Therefore, incorporation for Li into the kesterite lattice is more likely than for Na, K, or heavier alkali elements, which is in line with our findings. Furthermore, a decrease of the tetragonal distortion of the kesterite lattice is observed for the “high” Li samples (Figure S6, Supporting Information), which is also reported to be caused by Li incorporation into the kesterite lattice.^[22] The comparably small change in bandgap for Rb and Cs with the variation of Sn suggests that the composition of the kesterite phase is unchanged. Further investigations are needed to understand the stabilizing effect of Rb and Cs on the kesterite composition.

Figure 4a shows the efficiency for the “low” alkali content as well as without intentional alkali addition. The overall efficiencies for the samples containing light alkali elements are lower compared to the “high” alkali content case while for the heavy alkali elements even better efficiencies are observed. Furthermore, no obvious trend in the optimal Sn content for the different alkali elements is visible in contrast to the high alkali concentration results in Figure 1. Figure 4b illustrates the device efficiency for each alkali element for specific Sn concentrations yielding highest efficiency. It can be seen that the lighter alkali elements require higher concentrations in order to yield best device performance. For heavier alkali elements, a considerable improvement in the efficiency is already present at the low alkali content. At “high” alkali content Li, Na, and K

exhibit further increase in device performance in contrast to Rb and Cs which decrease in efficiency.

The effect of alkali content and alkali element size on the absorber layer morphology can be observed from the SEM cross sections in Figure 5 which show full devices including the $\text{CdS}/\text{i-ZnO}/\text{Al:ZnO}/\text{MgF}_2$ window layer. Figure 5a depicts the cross section of a representative sample without intentionally added alkali elements, which has a distinct bilayer structure with large grains on top and small grains in the lower part of the layer. Comparison of devices with different Sn contents (Figure S3, Supporting Information) confirms that no morphological changes are expected by variations in Sn concentration. Picture b)–e) display the evolution for increasing Li and Rb concentration. While for Li “high” alkali content is needed for obtaining large grains and favorable morphology while low alkali content is sufficient in the case Rb. Upon adding high Rb concentration the morphology changes to a dense, small grained layer that contains a high density of grain boundaries. Conclusively, the improvement in the morphology is largely correlated with the device performance.

The observation of morphology for each alkali element and concentration (Figure S4, Supporting Information) leads to a conclusion that the light alkali elements require higher concentration to reach a similar improvement in morphology as compared to the heavier alkali elements. This could be due to lower melting points of alkali-polyselenide phases of heavier alkali species as compared to lighter ones.^[24] Therefore, heavier alkali elements act more efficiently as a fluxing agent and, hence, lower concentrations are needed to achieve similar grain size improvements. A too high concentration leads to the fragmentation of the absorber layer and a dense but small-grained morphology with a high density of grain boundaries as shown for the Rb case. Therefore, each alkali element has its own optimal concentration at which it results in favorable morphology improvements and thus highest device performance. The trend of alkali content measured by ICP-MS in Figure 1b correlates with the increasing density of grain boundaries in the order of $\text{Na} < \text{K} < \text{Rb} < \text{Cs}$ that are present in the samples with high alkali concentrations, with an exception of Li, where the high

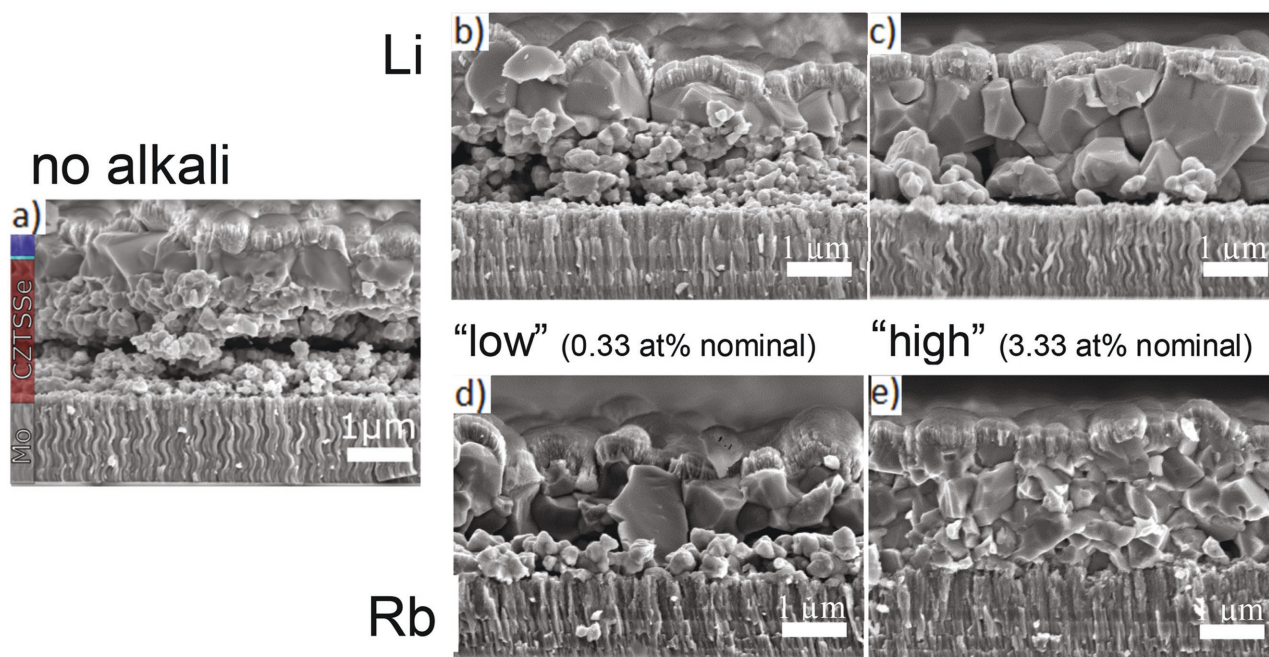


Figure 5. SEM cross sections of full devices including the window layer. a) Sample with no alkali treatment, b,c) samples with low and high Li treatment, and d,e) samples with low and high Rb treatment.

content of 0.76 at% is located inside the grains because Li can alloy with the kesterite phase.^[22,25]

In order to understand the device performance reduction for the samples at high Sn contents, XRD measurements on all devices were performed. The set of XRD patterns in **Figure 6a** displays the example of the “high” Na content for different nominal Sn concentrations. Reflexes originating from the kesterite phase are marked with red circles and additional reflexes at 31.6° and 56.5° indicate $\text{Mo}(\text{S,Se})_2$.^[26] The $\text{Sn}(\text{S,Se})_2$ secondary phase can be identified from the XRD patterns of samples with 33.3% nominal Sn content and more. Other secondary phases cannot be distinguished, however $\text{Zn}(\text{S,Se})$ and $\text{Cu}_2\text{Sn}(\text{S,Se})_3$ cannot be excluded since their reflexes coincide with those of CZTSSe.^[27] The XRD patterns of the other alkali elements and different concentrations look qualitatively similar with the exception of the appearance of $\text{Sn}(\text{S,Se})_2$ secondary phase. Therefore, the range from 12.5° to 17.5° was magnified in **Figure 6b** to present the appearance of $\text{Sn}(\text{S,Se})_2$ by the intensity of its 001 reflex, which is located at 14.42° for the pure selenide compound.^[28] Samples treated with heavier alkali elements exhibit $\text{Sn}(\text{S,Se})_2$ formation already at lower Sn contents, indicated by the appearance of the 001 Bragg reflex. Additionally, the XRD pattern of the layer with K exhibits a double reflex that may stem from $\text{Sn}(\text{S,Se})_2$ phases with different S/Se ratios. In the case of Cs, a small but invariant reflex appears for all Sn concentrations, but here the reflex overlaps with a possible secondary phase of Cs_2Se_3 that is also identified by its 112 reflex, which appears in the full XRD pattern (**Figure S5**, Supporting Information). Therefore, the $\text{Sn}(\text{S,Se})_2$ secondary phase for the high Cs content sample cannot be unambiguously identified. Cu_xSe secondary phase could not be identified from the XRD patterns of any sample, although the device PV parameters for low Sn content and a Cu/Sn ratio of

more than 2.0 exhibit a severe shunting behavior and formation of large, roundish grains typically associated with a Cu-rich material and formation of Cu_xSe .^[29] The following explanation for the appearance of secondary phases at different nominal Sn concentrations is suggested. The XRD results indicate that the alkali elements influence the composition of the kesterite phase. The kesterite composition correlates with the measured bandgap and Cu-poor kesterite exhibits a higher bandgap than Cu-rich kesterite.^[30,31] Utilizing the bandgap measurements from **Figure 3d** we deduce that the kesterite composition is less Cu-poor for Na compared to K for the same nominal Sn content. Conclusively, the remnant Sn not incorporated into the kesterite phase leads to the appearance of $\text{Sn}(\text{S,Se})_2$ secondary phase. For Rb and Cs, the bandgap barely changes suggesting a constant kesterite composition.

Figure 7 shows the EQE measurements of cells with none and “high” alkali content in the absorber layer. The EQE spectra of cells with none and the light alkali elements show qualitatively similar features from low to high nominal Sn content, which are a strong initial increase of the EQE followed by an increase in squareness and finally an overall decrease. The low EQE values at low Sn concentrations are due to shunting of the devices. The increase in squareness at intermediate Sn concentrations could be either an improvement in diffusion length of minority carriers or an increase in the space charge region width. Additionally, the bandgap, which is depicted in **Figure 3d**, is increasing steadily with increasing Sn concentration. In comparison, the EQE spectra of Rb and Cs show only a slight Sn dependency.

In order to further scrutinize the dependency of the optoelectronic properties on the Sn concentration, the apparent carrier concentration of all devices was determined by room-temperature CV measurements. In **Figure 8a–f**, the apparent carrier

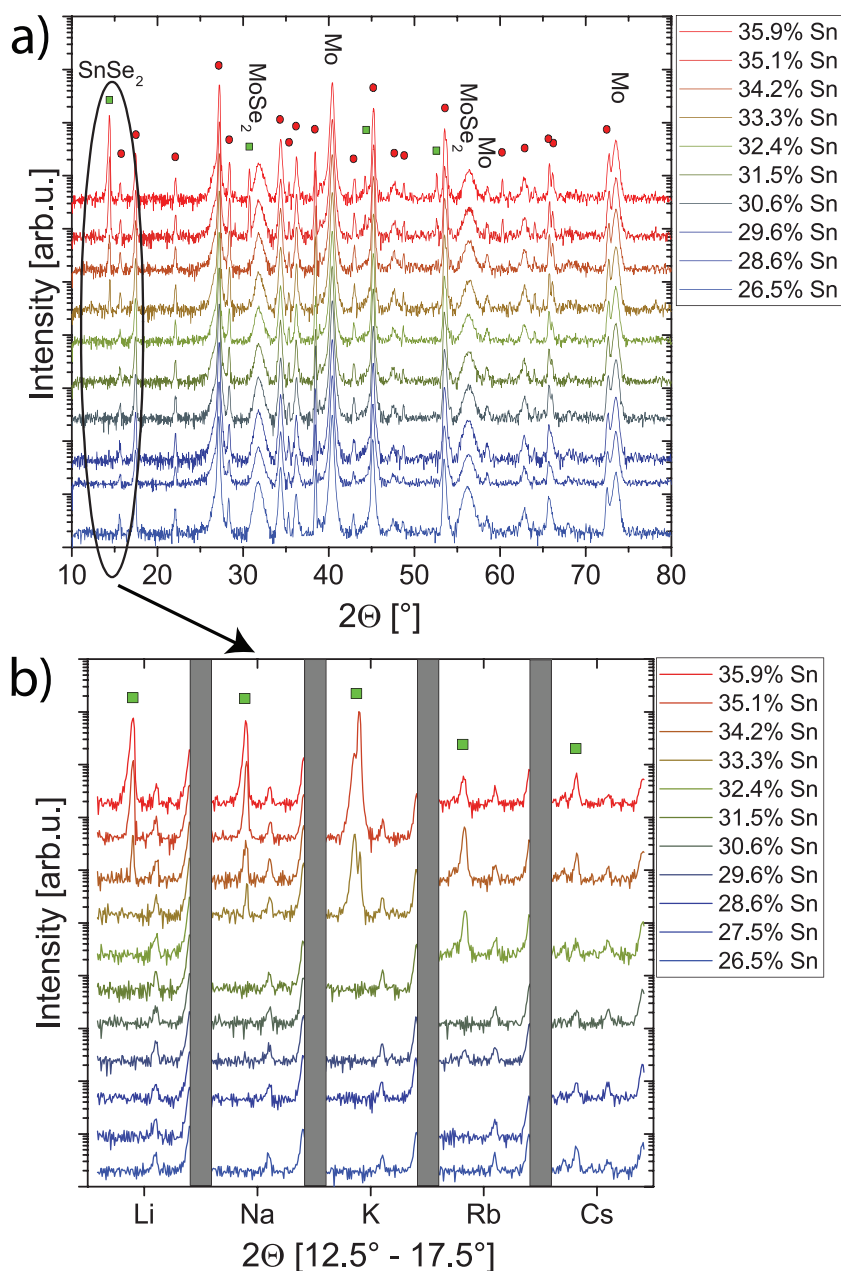


Figure 6. a) Set of XRD pattern for high Na content and different nominal Sn concentrations. Red dots indicate reflexes for kesterite (PDF01-070-8930) and green dots for $\text{Sn}(\text{S,Se})_2$ secondary phase. b) Range between 12.5° and 17.5° from the respective XRD pattern of none alkali treated and high alkali content samples.

concentration and space charge region width for representative sample sets with none and “high” alkali content are depicted. The sample sets for the lighter alkali elements exhibit a distinct correlation of the apparent carrier concentration with the Sn content. From $\approx 25\%$ Sn to 36% the apparent carrier concentration decreases by three orders of magnitudes from the range of $1 \times 10^{18} \text{ cm}^{-3}$ down to the range of $1 \times 10^{15} \text{ cm}^{-3}$. This change is directly correlated with the simultaneous increase in space charge region width from 20 to 40 nm to up to 500 nm. By assuming that the apparent carrier concentration is proportional to the doping concentration the evolution of EQE in

Figure 7 can be correlated to the CV results explaining the increase in squareness of the EQE by the widening of the space charge region (SCR).^[32] At the same time, the low carrier concentrations result in a weaker electric field in the SCR that eventually results in the reduction of the overall EQE for the whole wavelength region, which could be either caused by a barrier or a relatively low carrier lifetime in the SCR.^[33] The lower doping concentration results in a decrease of V_{OC} , but is obscured by the increase in bandgap that is obvious from the long wavelength EQE behavior in Figure 7.

The sample sets for Rb and Cs exhibit a comparably constant carrier concentration with $\approx 1 \times 10^{16}$ and $2 \times 10^{17} \text{ cm}^{-3}$, respectively. The steady carrier concentrations consequently lead to the similar EQE spectra for Rb and Cs. The constant doping concentrations of Rb and Cs are in agreement with the constant bandgap and PV parameters that are independent of the nominal Sn content.

Further device analysis by TRPL did not reveal any correlation of device parameters, alkali elements, and alkali concentration with the PL decay times (Figure S7, Supporting Information). The issue of deducing the minority carrier lifetime from TRPL measurement in kesterite solar cells has been recently described.^[34] Minority carrier trapping, surface effects, and energetic relaxation of carriers have been identified to severely affect the PL transient times, thus the measured PL decay times do not represent the real minority carrier lifetime in kesterite absorber layers.

Finally in **Figure 9**, the PV parameters, $J-V$, and EQE of the champion solar cell with a “high” Li content and 33.3% nominal Sn concentration are presented. The efficiency of 11.5% was determined by designated illumination area measurement including the front contact metal grid on a cell area of 0.29 cm^2 (active area efficiency without metal grid: 12.3%).

3. Conclusion

Our study reveals a complex dependency of metal ratios, alkali elements, and alkali concentration on the device performance in high-efficiency kesterite solar cells. Strikingly, from Li to Cs the nominal Sn concentration ($\text{Sn}/(\text{Cu}+\text{Zn}+\text{Sn})$) required for best device properties is reduced from 33.3 to 26.5% , that is more than 20% (relative). Additionally, the alkali concentration resulting in highest device efficiencies is lower by an order of magnitude for the heavy alkali elements (Rb, Cs) compared to the lighter ones (Li, Na, K). The PV parameters correlate with the changes in

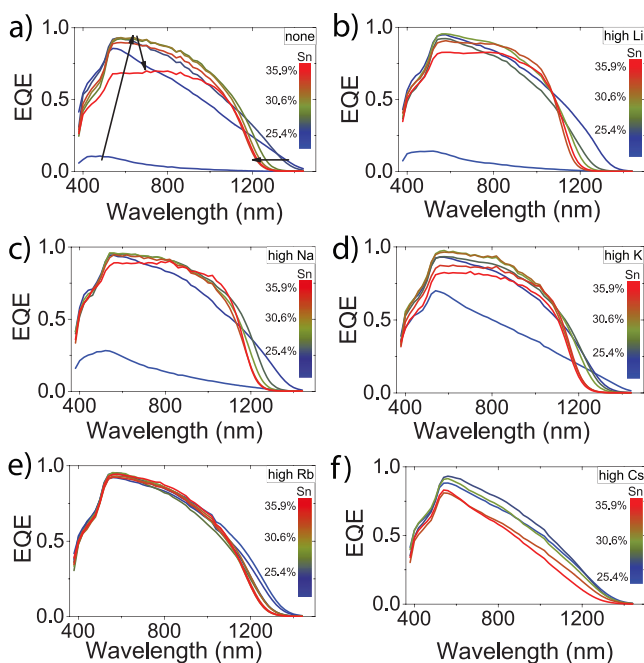


Figure 7. Set of EQE spectra for none alkali and high alkali treated samples. a–d) Samples exhibit similar qualitative features indicated by the arrows in (a). e,f) Only a minor influence of the variation in nominal Sn content on the EQE pattern is shown.

morphology with best devices exhibiting large grains throughout the whole absorber layer with low density of grain boundaries. The formation of tin diselenide secondary phases is significantly influenced by the type and concentration of alkali elements. As revealed by EQE and CV measurements the doping concentration varies by three orders of magnitude depending on the Sn content, except for high Rb and Cs content where a constant kesterite composition and therefore constant doping concentration is observed. A ranking of best device performances employing alkali treatment resulted in the order of $\text{Li} > \text{Na} > \text{K} > \text{Rb} > \text{Cs}$ based on the statistics of more than 700 individual cells. Finally, a champion device with 11.5% efficiency (12.3% active area) is presented using a “high” Li concentration with an optimized Sn content.

4. Experimental Section

The CZTSSe precursor solution consisted of thiourea (99%+, Sigma-Aldrich), $\text{SnCl}_2 \cdot 2\text{H}_2\text{O}$ (98%, Sigma-Aldrich), ZnCl_2 (99.99%, Alfa Aesar), and $\text{CuCl}_2 \cdot 2\text{H}_2\text{O}$ ($\geq 99.99\%$, Sigma-Aldrich), dissolved in dimethyl sulfoxide (99.9%, Alfa Aesar). The precursor solution contained 0, 10, or 100 mM of one of the following alkali chlorides: LiCl anhydrous (99.0%+, Fluka), NaCl (99.99%, Alfa Aesar), KCl (99.995%, Alfa Aesar), RbCl (99%, Alfa Aesar), and CsCl (99%, Alfa Aesar). A 200–300 nm thick SiO_x alkali diffusion barrier layer was sputtered onto a 1 mm thick soda-lime glass with a subsequent deposition of 1 μm of molybdenum. The precursor solution was spin-coated onto the Mo layer and dried on a hotplate at 320 °C in air. The spin-coating and drying steps were repeated 12 times in order to obtain the desired precursor film thickness of 1.5 μm . All samples were annealed in an RTP furnace (Annealsys AS ONE 150) inside a closed graphite box with selenium pellets (800 mg). The temperature gradient employed for annealing was the three-stage process with holding at 300, 500, and 550 °C. After selenization the

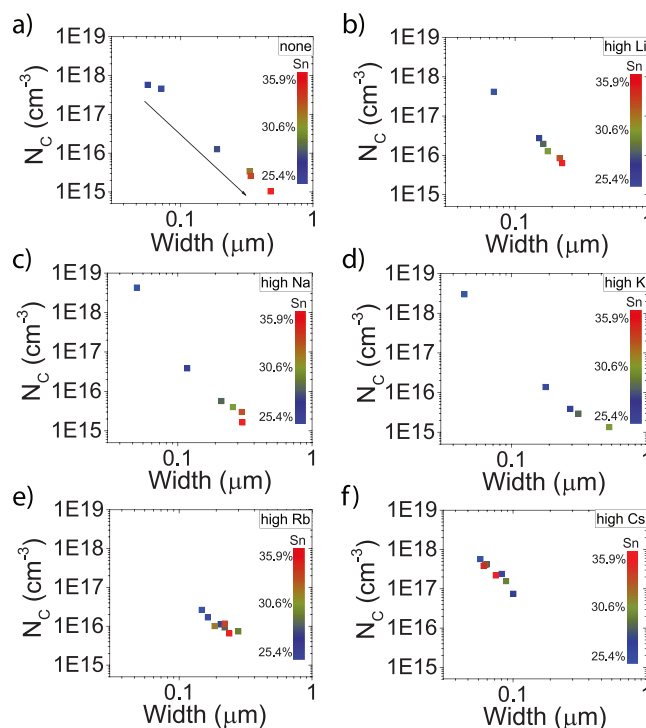


Figure 8. The apparent carrier concentration and space charge region width for representative sample sets with none alkali and high alkali content samples, calculated from room-temperature CV measurements.

absorbers were immersed for 30 s in a 10 wt% KCN solution in order to remove copper-rich phases and clean the surface from contaminations and oxides. A 50–70 nm thick CdS buffer layer was deposited by chemical bath deposition, and 70 nm/250 nm i-ZnO/Al:ZnO bilayer was sputtered. A Ni/Al top grid and an antireflection coating of MgF_2 were deposited by e-beam evaporation. Individual solar cells were mechanically scribed to an area of $0.30 \pm 0.02 \text{ cm}^2$.

Metal ratios were measured by XRF calibrated by ICP-MS. For ICP-MS analysis, $\approx 1 \text{ cm}^2$ of the kesterite solar cells were etched for 60 s in 5 wt% acetic acid solution in order to remove the window layer. Then kesterite

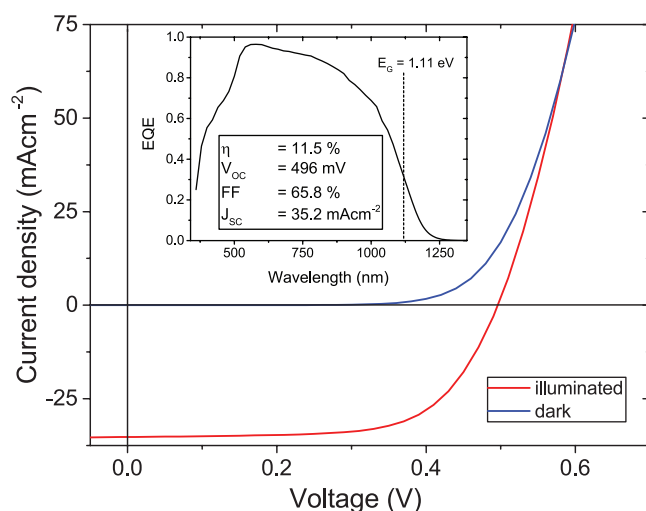


Figure 9. J – V , EQE, and PV parameters of the champion device with high Li content and 33.3% nominal Sn content. The cell exhibits a high bandgap of $E_g = 1.11 \text{ eV}$ due to Li incorporation into the kesterite phase.

absorber material was detached from the thin-film solar cell at the Mo/CZTSSe interface, directly transferred into 50 mL trace metal-free polyethylene tubes and fully dissolved in a mixture of 2.5 mL H₂O₂ 30% MERCK suprapure, 4 mL HNO₃ 67% MERCK ultrapure, and 2.5 mL HCl 32% MERCK ultrapure. After filling to 25 mL with 18 MΩ cm deionized water, the sample was diluted 1:10 with 18 MΩ cm deionized water for analysis. Metal determinations were performed on an Agilent 8800 triple quadrupole ICP-MS with different reaction modes such as He and O₂ and external calibration using certified metal standards (1000 µg mL⁻¹, Alfa Aesar Specpure). For quality assurance, analysis of reference materials and spiking experiments were performed, with recoveries between 90 and 110%.

SEM measurements were done on a Hitachi S-4800 electron microscope, XRD patterns were recorded in $2\theta/\theta$ scan mode using a Bruker D8 diffractometer with CuK α radiation ($\lambda = 1.5418$ Å, beam voltage: 40 kV, beam current: 40 mA, calibrated using Si100 and Si111 single crystals), a step size of 0.04°, and a scan rate of 0.5 s step⁻¹ for the full pattern and a step size of 0.004° and a scan rate of 2 s step⁻¹ for the detailed pattern. The *J*-*V* characterization was performed under standard test conditions (100 mW cm⁻², 25 °C, AM1.5G) using a solar simulator calibrated with a certified Si diode. The EQE spectra were recorded using a chopped white light source (900 W halogen lamp) with a LOT MSH-300 monochromator, which was calibrated with certified Si and Ge diodes. The illuminated area on the sample was 0.1 cm² including grid lines. Room-temperature CV measurements were carried out with a LCR meter from Agilent (E4990A) with an AC voltage of 30 mV at 25 °C. Room-temperature TRPL decay curves were recorded on a FT300 fluorescence lifetime spectrometer from PicoQuant with a 639 nm pulsed diode laser as excitation source (pulse width 90 ps, repetition rate 10 MHz) and a thermoelectric cooled Hamamatsu NIR-PMT module H10330A-45 (rise time 0.9 ns, transit time spread 0.4 ns).

Supporting Information

Supporting Information is available from the Wiley Online Library or from the author.

Acknowledgements

This research was supported by the Framework 7 program under the project KESTCELLS (FP7-PEOPLE-2012-ITN-316488) and the Horizon2020 program under the project STARCELLS (H2020-NMBP-03-2016-720907). S.H. thanks J. Marquez for discussion on the XRD measurements. C.A. acknowledges support from the Swiss National Science Foundation, project IZLIZ2_157140/1. The authors would also like to thank the whole team of the Laboratory for Thin Films and Photovoltaics.

Conflict of Interest

The authors declare no conflict of interest.

Keywords

alkali doping, kesterite, solution processing, thin-film solar cells

Received: June 28, 2017

Revised: August 2, 2017

Published online: October 4, 2017

- [1] X. Yi, presented at DGIST, PVSEC Singapore 2016, Singapore, October 2016.
- [2] S. Bourdais, C. Choné, B. Delatouche, A. Jacob, G. Larramona, C. Moisan, A. Lafond, F. Donatini, G. Rey, S. Siebentritt, A. Walsh, G. Dennler, *Adv. Energy Mater.* **2016**, 6, 1502276.
- [3] T. Abzieher, T. Schnabel, M. Hetterich, M. Powalla, E. Ahlswede, *Phys. Status Solidi A* **2016**, 213, 1039.
- [4] T. Gershon, B. Shin, N. Bojarczuk, M. Hopstaken, D. B. Mitzi, S. Guha, *Adv. Energy Mater.* **2015**, 5, 1400849.
- [5] C. M. Sutter-Fella, J. A. Stükelberger, H. Hagendorfer, F. La Mattina, L. Kranz, S. Nishiwaki, A. R. Uhl, Y. E. Romanyuk, A. N. Tiwari, *Chem. Mater.* **2014**, 26, 1420.
- [6] I. Repins, C. Beall, N. Vora, C. DeHart, D. Kuciauskas, P. Dippo, B. To, J. Mann, W.-C. Hsu, A. Goodrich, R. Noufi, *Sol. Energy Mater. Sol. Cells* **2012**, 101, 154.
- [7] H. Xin, S. M. Vorpahl, A. D. Collord, I. L. Braly, A. R. Uhl, B. W. Krueger, D. S. Ginger, H. W. Hillhouse, *Phys. Chem. Chem. Phys.* **2015**, 17, 23859.
- [8] Z. Tong, C. Yan, Z. Su, F. Zeng, J. Yang, Y. Li, L. Jiang, Y. Lai, F. Liu, *Appl. Phys. Lett.* **2014**, 105, 223903.
- [9] W. Li, Z. Su, J. M. R. Tan, S. Y. Chiam, H. L. Seng, S. Magdassi, L. H. Wong, *Chem. Mater.* **2017**, 29, 4273.
- [10] A. Mule, B. Vermang, M. Sylvestre, G. Brammertz, S. Ranjbar, T. Schnabel, N. Gampa, M. Meuris, J. Poortmans, *Thin Solid Films* **2017**, 633, 156.
- [11] Y.-T. Hsieh, Q. Han, C. Jiang, T.-B. Song, H. Chen, L. Meng, H. Zhou, Y. Yang, *Adv. Energy Mater.* **2016**, 6, 1502386.
- [12] G. Altamura, M. Wang, K.-L. Choy, *Sci. Rep.* **2016**, 6, 22109.
- [13] S. López-Marino, Y. Sánchez, M. Espíndola-Rodríguez, X. Alcobé, H. Xie, M. Neuschitzer, I. Becerril, S. Giraldo, M. Dimitrievska, M. Placidi, L. Fourdrinier, V. Izquierdo-Roca, A. Pérez-Rodríguez, E. Saucedo, *J. Mater. Chem. A* **2016**, 4, 1895.
- [14] S. G. Haass, M. Diethelm, M. Werner, B. Bissig, Y. E. Romanyuk, A. N. Tiwari, *Adv. Energy Mater.* **2015**, 5, 1500712.
- [15] M. Werner, C. M. Sutter-Fella, H. Hagendorfer, Y. E. Romanyuk, A. N. Tiwari, *Phys. Status Solidi A* **2015**, 212, 116.
- [16] E. Cadel, N. Barreau, J. Kessler, P. Pareige, *Acta Mater.* **2010**, 58, 2634.
- [17] P. Reinhard, B. Bissig, F. Pianezzi, E. Avancini, H. Hagendorfer, D. Keller, P. Fuchs, M. Döbeli, C. Vigo, P. Crivelli, S. Nishiwaki, S. Buecheler, A. N. Tiwari, *Chem. Mater.* **2015**, 27, 5755.
- [18] H. Xie, Y. Sánchez, S. López-Marino, M. Espíndola-Rodríguez, M. Neuschitzer, D. Sylla, A. Fairbrother, V. Izquierdo-Roca, A. Pérez-Rodríguez, E. Saucedo, *ACS Appl. Mater. Interfaces* **2014**, 6, 12744.
- [19] S. Siebentritt, S. Schorr, *Prog. Photovolt.: Res. Appl.* **2012**, 20, 512.
- [20] T. Gokmen, O. Gunawan, T. K. Todorov, D. B. Mitzi, *Appl. Phys. Lett.* **2013**, 103, 103506.
- [21] G. Rey, A. Redinger, J. Sendler, T. P. Weiss, M. Thevenin, M. Guennou, B. E. Adib, S. Siebentritt, *Appl. Phys. Lett.* **2014**, 105, 112106.
- [22] A. Lafond, C. Guillot-Deudon, J. Vidal, M. Paris, C. La, S. Jobic, *Inorg. Chem.* **2017**, 56, 2712.
- [23] T. Maeda, A. Kawabata, T. Wada, *Phys. Status Solidi C* **2015**, 12, 631.
- [24] J. Sangster, A. D. Pelton, *J. Phase Equilib.* **1997**, 18, 173.
- [25] Y. Yang, X. Kang, L. Huang, D. Pan, *ACS Appl. Mater. Interfaces* **2016**, 8, 5308.
- [26] B. Shin, N. A. Bojarczuk, S. Guha, *Appl. Phys. Lett.* **2013**, 102, 091907.
- [27] P. J. Dale, K. Hoenes, J. Scragg, S. Siebentritt, in *2009 34th IEEE Photovoltaic Specialists Conf., PVSC, IEEE, Philadelphia, PA, USA, 2009*, pp. 2080–2085.
- [28] K. Liu, H. Liu, J. Wang, L. Feng, *Mater. Lett.* **2009**, 63, 512.

- [29] W. C. Hsu, I. Repins, C. Beall, G. Teeter, C. DeHart, B. To, Y. Yang, R. Noufi, in *2012 38th IEEE Photovoltaic Specialists Conf.*, IEEE, Austin, TX, USA, **2012**, pp. 674–677.
- [30] J. Márquez, M. Neuschitzer, M. Dimitrievska, R. Gunder, S. Haass, M. Werner, Y. E. Romanyuk, S. Schorr, N. M. Pearsall, I. Forbes, *Sol. Energy Mater. Sol. Cells* **2016**, 144, 579.
- [31] C. Krämmmer, C. Huber, C. Zimmermann, M. Lang, T. Schnabel, T. Abzieher, E. Ahlswede, H. Kalt, M. Hetterich, *Appl. Phys. Lett.* **2014**, 105, 262104.
- [32] *Advanced Characterization Techniques for Thin Film Solar Cells* (Eds: D. Abou-Ras, T. Kirchartz, U. Rau), Wiley-VCH, Weinheim, Germany, **2016**.
- [33] R. Scheer, H.-W. Schock, *Chalcogenide Photovoltaics: Physics, Technologies, and Thin Film Devices*, Wiley, Weinheim, Germany, **2011**.
- [34] C. J. Hages, A. Redinger, S. Levchenko, H. Hempel, M. J. Koeper, R. Agrawal, D. Greiner, C. A. Kaufmann, T. Unold, *Adv. Energy Mater.* **2017**, <https://doi.org/10.1002/aenm.201700167>.